Design and Performance Comparison of Vernier and Conventional PM Synchronous Wind Generators

Pushman M. Tlali [ID] , *Member, IEEE*, Rong-Jie Wang [ID] , *Senior Member, IEEE*, Stiaan Gerber [ID] , *Member, IEEE*, Christoff Daniel Botha [ID] , and Maarten J. Kamper [ID] , *Senior Member, IEEE*

Abstract—In recent years, the permanent magnet vernier machine (PMVM) has attracted much attention in the research community. Many studies have shown that PMVMs possess superior torque density and are suitable for high-torque and low-speed applications. Some of them compared PMVMs with the direct-drive permanent magnet synchronous machines (PMSMs), but these studies focused mainly on sub-kW power levels. There is little work in the literature that conducted the comprehensive evaluation of PMVM technology for more specific applications. This article presents the design optimization of a 15-kW surface-mounted PMVM and its comparison with an equivalent conventional PMSM for wind generator applications. It attempts to objectively weigh the relative merits of the two wind generator systems and outline their respective advantages and disadvantages. For validation purposes, an optimally designed 15-kW PMVM was constructed and experimentally evaluated, which is one of the largest PMVM prototypes ever reported in the literature. It shows that the PMVM can be a competitive alternative to the PMSM for this application.

Index Terms—Design optimization, direct-drive wind generator, finite-element analysis (FEA), magnetic gearing effect, permanent magnet, vernier machines.

I. INTRODUCTION

WITH the steady growth of the global demand for wind energy, the size and output capacity of wind turbines have also been increasing over the years [1], which has made it more challenging to mount a nacelle on the top of a tower. Thus, mechanically geared generator systems are still popular options although they are prone to reliability issues. For applications with serviceability issues (e.g., offshore wind farms), the direct-drive permanent magnet synchronous machine (PMSM) remains a favored option despite its known heavy weight and large size in comparison to the geared systems [2], [3]. In recent years, the permanent magnet vernier machine (PMVM) has emerged as

an attractive alternative to conventional direct-drive PMSMs for wind power applications [4]–[6]. By virtue of their inherent magnetic gearing effects, PMVMs render superior torque density compared to PMSMs while they also possess the same structural simplicity [7]–[9]. Some comparative studies between these two machine types are reported in [6] and [10]–[13]. However, these studies were generally conducted on small (sub-kW) PMVM designs and have little relevance to higher capacity wind power applications. Furthermore, there is a lack of literature focused on more comprehensive evaluation of PMVM technology for wind generator applications.

This article is the extended version of [5], which was a modest first attempt on the design, comparison, and performance evaluation of a surface-mounted PMVM for wind power applications. The considered wind power system, rated at 15 kW, was designed for the South African Antarctic research base SANAE IV. In this updated article, the principles of the PMVM are briefly reviewed in Section II, a comparative study of selected PMVM topologies (described in Section III) was conducted using finite-element (FE) analysis (FEA) and numerical optimization to investigate their performance capabilities, described in Section IV. Unlike in [5], the study was carried out based on the specifications of an optimally designed 15 kW direct-drive PMSM. The primary objective of the optimization was to minimize the electromagnetic active mass of the PMVMs, while satisfying the required performance constraints. Consequently, one of the best pole/slot combinations is chosen to be further analyzed in Section V. The viability of using PMVM technology for wind power applications was then evaluated by comparing it with the PMSM in terms of performance, costs, and weight. To validate the results presented in [5], the designed 15 kW PMVM was constructed, tested, and compared with the benchmark PMSM. Finally, relevant conclusions are drawn in Section VI.

II. OPERATING PRINCIPLES OF PMVMs

The operational principle of the PMVM is similar to that of flux modulated magnetic gears, whereby the high-speed (low-pole-count) PM poles are magnetically coupled to the low-speed (high-pole-count) PM poles through modulation by the ferromagnetic pole pieces. In PMVMs, the high-speed field harmonics are produced by the armature currents, while the low-speed poles are created by the rotor PMs. Basic structure configurations of PMVM are presented in Fig. 1 where it can be seen that the stator teeth can also act as the flux modulation pieces
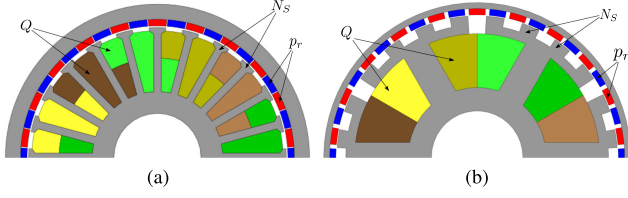
Fig. 1. Typical structures of PMVM machines: (a) conventional overlap-winding PMVM; (b) tooth-concentrated, split-tooth PMVM.

Fig. 2. Illustration of open-circuit air-gap magnetic flux density modulation in PMVM.

[see Fig. 1(a)] or the teeth tips can be split to create numerous pieces of flux modulation components [see Fig. 1(b)]. Also, the stator's magnetic pole pairs number is always less than that of the rotor PMs. To enable the magnetic gearing effect, the number of ferromagnetic pole pieces (N_s), armature magnetic pole pairs (p_s), and rotor PM pole pairs (p_r) must satisfy the following relationship [7], [14]:

$$N_s = p_r + p_s \quad \text{or} \quad N_s = p_r - p_s. \tag{1}$$

By assuming that iron's relative permeability is infinite, and that the PMs are uniformly magnetized in the radial direction for radial flux machines, the open-circuit air-gap flux density distribution along the angular periphery of the rotor (θ) can then be described as [7], [14], [15]:

$$B_{PM}(\theta, t) = F_{PM}(\theta, t) \times \Lambda(\theta)$$
$$\cong [F_{PM1} \cos \{p_r(\theta - \omega_r t)\}] \times [\Lambda_0 - \Lambda_1 \cos(N_s\theta)] \tag{2}$$

where F_{PM} and Λ are the PMs magnetomotive force (MMF) distribution and the air-gap permeance function, respectively. For analysis purposes, the effects of high-order harmonics may be ignored. It suffices to approximate B_{PM} with just the average and the fundamental harmonic components of both F_{PM} and Λ, which then gives the following expression:

$$B_{PM}(\theta, t) \cong B_{PM0} \cos \{p_r(\theta - \omega_r t)\}$$
$$- \frac{B_{PM1}}{2} \left\{ \begin{array}{l} \cos \{(N_s - p_r)\theta - p_r\omega_r t\} \\ + \cos \{(N_s + p_r)\theta - p_r\omega_r t\} \end{array} \right\} \tag{3}$$

where $B_{PM0} = F_{PM1}\Lambda_0$, $B_{PM1} = F_{PM1}\Lambda_1$, and $\frac{d}{dt}\theta_r = \omega_r$.

An illustration of the flux modulation effect in PMVM, as described by (3), is provided in Fig. 2. It shows a 10-pole-pair field harmonic from a PM rotor being modulated by the 12 modulation pieces. On examining both (3) and Fig. 2 in conjunction with (1), it can be seen that the resultant air-gap flux density distribution has three major components, being the term that has equal harmonic order and rotates synchronously with the PM rotor and the two other terms produced by the modulation effect of the ferromagnetic pole pieces. It is important to realize that the stator winding would have to be designed such that the fundamental MMF harmonic generated by the armature coil current bears similar spacial period to one of these modulated terms. Thus, the engagement of these two field harmonic components results in steady torque transmission between the rotor and stator, even though they have different number of pole pairs.
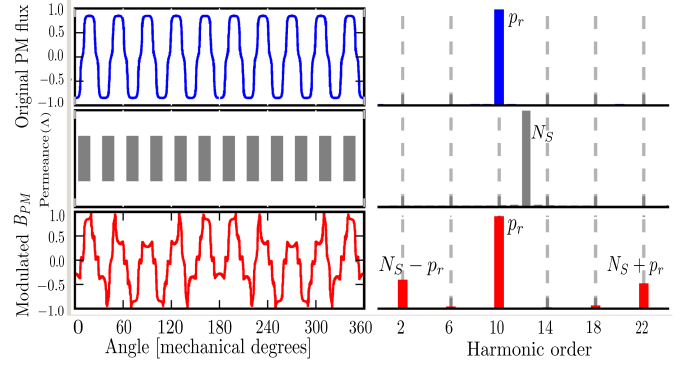
Integrating (3) relative to the angular distance of the armature coil would give the per phase open-circuit flux linkage. Consequently, the change of flux linkage with respect to time results in the induced electromotive force (EMF)

$$E_{ph(rms)} = K_{w1} N_{ph} D_g L_{\text{stk}} \omega_r \left[B_{PM0} + \frac{p_r}{p_s} \frac{B_{PM1}}{2} \right] \tag{4}$$

where D_g, L_{stk}, N_{ph}, and K_{w1} are the air-gap diameter, machine active stack length, number of turns per phase, and the fundamental winding factor, respectively. The presence of two voltage components is now evident in the developed voltage expression. The first term is equivalent to the component found in classical synchronous machines, while the second term is due to the vernier effect. With the numbers of pole pairs and ferromagnetic pole pieces chosen according to the first scenario of (1), the two EMF components add up together, contributing to larger voltage production [7]. With the induced voltage and phase current (I_{ph}) known, the air-gap torque for a three-phase PMVM is then formulated as

$$T_q = K_{w1} N_{ph} I_{ph} D_g L_{\text{stk}} \left[B_{PM0} + \frac{p_r}{p_s} \frac{B_{PM1}}{2} \right]. \tag{5}$$

It can be clearly seen from (5) that a PM rotor-to-stator magnetic pole-ratio factor (p_r/p_s) also appears to proportionately increase the torque.

III. Considered PMVM Configurations

PMVMs of various configurations can be realized, each characterized by different merits. This study focused on the common PMVMs with single-stator and single-rotor configurations shown in Fig. 1. The choice of the number of stator slots, armature and rotor pole pairs is very important as this determines the machine's gear ratio (G_r) and operating frequency for a given input speed. As a preliminary design exercise to find a suitable pole ratio to work with, a survey was taken whereby a series of 15 kW PMVMs with various pole/slot combinations and pole ratios were optimized under the same design constraints. Again, in order to select the best PMVM configuration, the optimization was done for the following two different PMVM types:

1) conventional PMVM (with overlap-winding) [see Fig. 1(a)];

TABLE I
INVESTIGATED POLE–SLOT COMBINATIONS FOR OVERLAP-WINDING PMVMS

p_s	Pole-ratio = 5			Pole-ratio = 8			Pole-ratio = 11			Pole-ratio = 14			Pole-ratio = 17			Pole-ratio = 20		
	Q	p_r	q	Q	p_r	q	Q	p_r	q	Q	p_r	q	Q	p_r	q	Q	p_r	q
1	6	5	1.0	9	8	1.5	12	11	2.0	15	14	2.5	18	17	3.0	21	20	3.5
2	12	10	1.0	18	16	1.5	24	22	2.0	30	28	2.5	36	34	3.0	42	40	3.5
3	18	15	1.0	27	24	1.5	36	33	2.0	45	42	2.5	54	51	3.0	63	60	3.5

TABLE II
INVESTIGATED POLE–SLOT COMBINATIONS FOR TOOTH-CONCENTRATED-WINDING PMVMS

p_s	Pole-ratio = 5				Pole-ratio = 8				Pole-ratio = 11				Pole-ratio = 14				Pole-ratio = 17				Pole-ratio = 20			
	Q	N_s	p_r	q	Q	N_s	p_r	q	Q	N_s	p_r	q	Q	N_s	p_r	q	Q	N_s	p_r	q	Q	N_s	p_r	q
1	3	6	5	0.5	3	9	8	0.5	6	12	11	1.0	3	15	14	0.5	9	18	17	1.5	3	21	20	0.5
2	6	12	10	0.5	9	18	16	0.75	12	24	22	1.0	15	30	28	1.25	6	36	34	0.5	21	42	40	1.75
3	9	18	15	0.5	9	27	24	0.5	18	36	33	1.0	9	45	42	0.5	27	54	51	1.5	9	63	60	0.5

TABLE III
DESIGN SPECIFICATIONS

Parameter	Value
Output power	15 kW
Operating speed	150 r/min
Efficiency	94 %
Power factor	≥ 0.6
Current density	5 A/mm^2
Air-gap length	1.5 mm
Aspect ratio (L_{stk}/D_{out})	0.2 - 0.6
Slot-fill factor	0.4
Lamination steel grade	M470-50A
Permanent magnet grade	N48H
Permanent magnet mass	≤ 9 kg
Outer diameter (D_{out})	< 655 mm

2) split-tooth PMVM (with tooth-concentrated nonoverlap-winding) [see Fig. 1(b)].

All the investigated pole/slot combinations are listed in Tables I and II for overlap-winding and tooth-concentrated machines, respectively. Considered machine designs were selected to have gear ratios (G_r) spanning from 5 up to 20 increasing in steps of 3, and the number of stator pole pairs are 1, 2, and 3. As explained in [5], while the number of stator slots or teeth (Q) is the same as the number of modulating pieces (N_s) in conventional overlap-winding PMVMs, this is not the case in tooth-concentrated-winding machines. For the latter, the designer has to separately choose the number of stator slots, which, in combination with the stator pole pairs, will have the best possible winding factor, as outlined in other studies for this winding type [16], [17]. In addition, the number of stator teeth must be a factor of the modulator pole pieces in tooth-split PMVMs.

IV. DESIGN OPTIMIZATION

The objective of the design optimization process was to minimize each machine's total active mass while meeting specifications on the output power, efficiency, power factor, and current density. The main design specifications for this study are listed in Table III. The machines were designed for an output power of 15 kW with at least 94% efficiency at the rated speed of 150 r/min. Considering the manufacturability of the winding, the slot-fill factor was chosen as 0.4.

A limit was imposed on the current density to ensure that the winding temperature is within acceptable limits. The maximum PM mass was also limited to 9 kg. Since PMVMs are usually featured with poor power factors, a minimum constraint of 0.6 was added on the PF to ensure reasonable designs for comparative purposes. The maximum outer diameter was constrained to be less than or equal to that of a benchmark PMSM. The optimization process was performed with two-dimensional (2-D) FE static analyses of the machines. In order to reduce the number of design variables, a constant current angle of $\theta = 90°$ was assumed. In practice, a current angle slightly larger than $90°$ is usually optimal for surface-mounted PM machines. The modified method of feasible directions (MMFD) algorithm in the VisualDOC optimization suite from VR&D Inc. [18] was employed for the optimization. VisualDOC calls external Python scripts which run the finite element method (FEM) analysis using an in-house FEM simulation package. Thus, the constrained optimization problem was formulated as follows:

$$\text{Minimize:} \quad F(\mathbf{X}) = M_{\text{Total}}$$
$$\text{Subject to:} \quad P_{\text{out}} \geq 15 \text{ kW}$$
$$\eta \geq 94\%$$
$$\text{PF} \geq 0.6$$
$$J \leq 5 \text{ A/mm}^2$$

where $\mathbf{X}$ represents the vector of geometric variables illustrated in Fig. 3 with angle ratios defined as follows, including the axial stack length of the machine:

$$\theta_{pm\_p} = \frac{\pi}{p_r} \quad \theta_{sp} = \frac{2\pi}{Q}$$
$$\sigma_{pm} = \frac{\theta_{pm\_s}}{\theta_{pm\_p}} \quad \sigma_s = \frac{\theta_s}{\theta_{sp}} \quad \sigma_{so} = \frac{\theta_{so}}{\theta_s}$$
$$\theta_{mp} = \frac{2\pi}{N_s} \quad \sigma_{mo} = \frac{\theta_{mo}}{\theta_{mp}} \quad \sigma_{mi} = \frac{\theta_{mi}}{\theta_{mp}}. \tag{6}$$

During the optimization process, core loss, end-winding length, end-winding inductance, and resistance were calculated
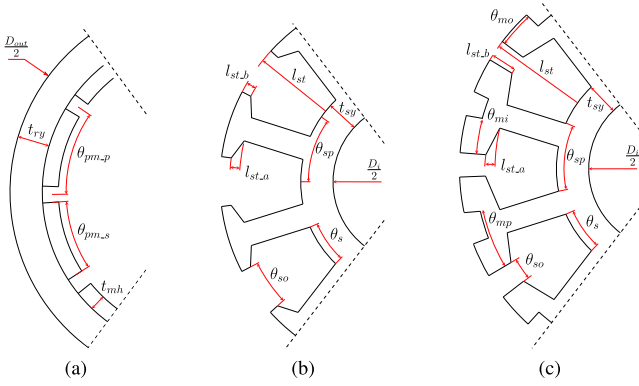
Fig. 3. Machine geometric optimization variables: (a) rotor; (b) conventional stator; and (c) split-tooth stator.

using analytical equations. These quantities were used to supplement the results obtained from the 2-D FEA static solutions such that their effect is accounted for in the performance analysis.

A. Electromagnetic Active Mass

The total active masses as a function of the gear ratios for the two PMVM configurations are quantitatively compared in Figs. 4(a) and 5(a). It can be observed that as the gear ratio increases, the total active mass initially decreases before this downward trend ceases at a certain gear ratio, after which the mass stays constant or even increases again. The reason for this is that the higher gear ratio designs have a large number of rotor pole pairs, which encourages excess PM leakage flux and consequently, poorer performance. In addition, a higher gear ratio also implies a higher operational frequency for the same input speed, which results in increased core losses. Since the minimum efficiency requirement has to be fulfilled in the optimization, a design with high core loss would respond by increasing the rotor and stator yoke thicknesses to reduce flux density magnitudes in the affected regions, leading to heavier designs.

Another noticeable trend is that combinations with $p_s = 1$ generally lead to the heaviest designs due to their thick stator and rotor yokes. This is more apparent in tooth-concentrated winding machines where some of the combinations on the lower scale of the gear ratio ($G_r = 5$ and 8) could not even meet the optimization constraints, hence omitted from the graphs. For overlap-winding machines with stator magnetic pole pairs equal to 2 and 3, the mass begins to be constant at $G_r = 11$ and upward, whereas it slowly increases for tooth-concentrated machines.

B. Power Factor

When considering the power factor, Figs. 4(b) and 5(b) show that it does not necessarily follow a uniform trend against the rising gear ratio, although on average, most machines on the high end have lower power factor than those on the lower side of the G_r scale. This phenomenon can be better explained by the simplified power factor expression (7), whereby the pole ratio appears on the denominator of the equation and its influence on

X_{sg} outweighs that of E_{ph} [19]. Consequently, it can be realized that the power factor has an indirect inverse proportionality to the gear ratio

$$X_{sg} = \omega_r p_r L_{sg} = \omega_r \frac{p_r}{p_s} \frac{m}{2} \frac{\pi \mu_0 N_{ph}^2 L_{stk} D_g}{4 p_s g} K_{w1}$$

$$\text{PF} = \frac{1}{\sqrt{1 + \left(\frac{X_{sg} I_{ph}}{E_{ph}}\right)}} \tag{7}$$

where PF, L_{sg}, and X_{sg} are the power factor and synchronous inductance and reactance, respectively; m is winding phase number, g is the effective air-gap length, and μ_0 is the free space permeability.

Furthermore, this may also be attributed to the fact that designs with larger G_r values are more prone to excessive flux leakage. Based on the comparison between the two machine types, overlap-winding PMVMs show better power factor relative to the tooth-concentrated winding machine type. Besides, most of the tooth-concentrated winding PMVMs are characterized by poor winding factor. In general, the results in Figs. 4(b) and 5(b) demonstrate that the PMVMs' power factor at this output power capacity can hardly reach above 0.7. Thus, G_r does not only improve on the machines' torque capacity, but also scales up the reactance as proved by (7), leading to poor power factors.

C. Torque Quality

In PM excited and slotted iron core machines, cogging and torque ripple are caused by the interaction of PM field with the varying stator permeance and stator electromagnetic field harmonics, respectively. A good indication of the severity of these undesirable characteristics can be obtained by examining the lowest common multiple (LCM) between the number of PM pole pairs and the number of stator teeth [20]. Theoretically, a higher LCM value is more favorable since it predicts a lower degree of cogging or ripple torque. In this study, the torque ripple characteristics [shown in Figs. 4(c) and 5(c)] were calculated using the multistep static FEA. It is interesting to note that the torque ripple is very low for most of the overlap winding PMVMs without any special strategy being applied to minimize the torque ripple. This inherent feature is a result of the high LCM values between the stator pole pairs and slot numbers, and is one strong advantage of this type of machine. On the other hand, the combinations with $G_r = 5$ have the worst torque ripples across all the evaluated designs, which is because of their low LCMs of the stator teeth and rotor pole pairs as also shown in [21] and [22]. The tooth-concentrated winding PMVMs show significant torque ripple with most designs above the 5% mark. This is to be expected since this type of winding is well known to be rich in magnetic field harmonics.

V. COMPARISON OF PMSM AND PMVM

A. FE Design of Selected PMVM

A previously optimized PMSM design [23] was used as a benchmark against which the best PMVM design could be compared. In order to do a fair comparison study on these two
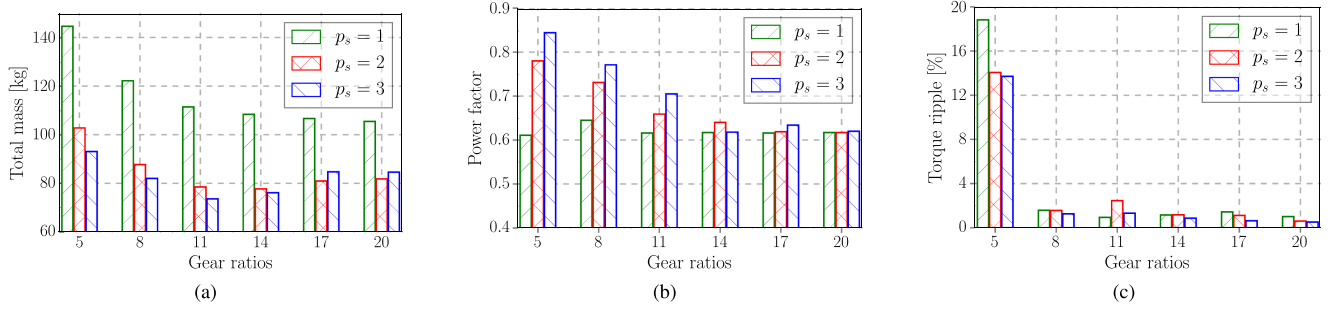
Fig. 4. Conventional overlap-winding PMVM. (a) Total active mass versus gear ratio. (b) Power factor versus gear ratio. (c) Torque ripple versus gear ratio.
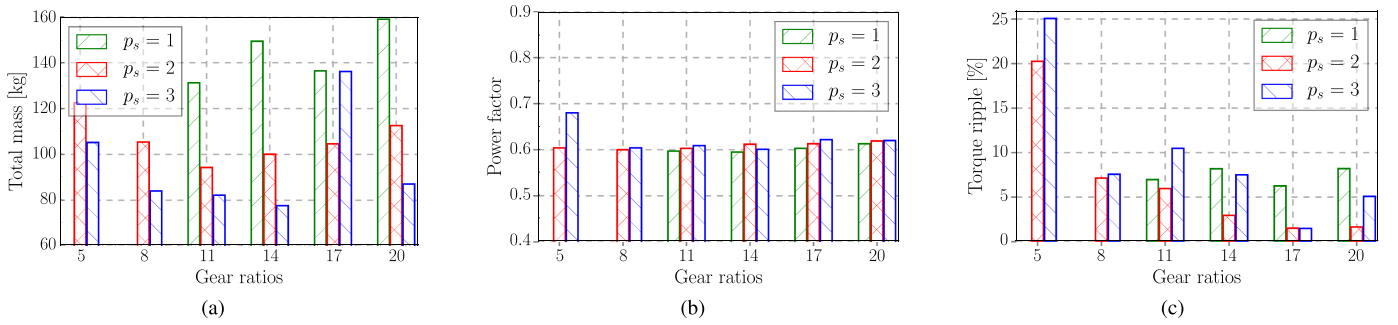

Fig. 5. Tooth-concentrated, split-tooth PMVMs. (a) Total active mass versus gear ratio. (b) Power factor versus gear ratio. (c) Torque ripple versus gear ratio.

TABLE IV
COMPARED MACHINE PROPERTIES

Parameter	PMSM	PMVM
Stator slots	48	36
Winding poles	40	6
Rotor poles	40	66
Rated frequency (Hz)	50	82.5
Winding type	Non-overlap	Overlapping

machines, the rated operating speed and output power were kept equal as 150 r/min and 15 kW, respectively. According to the results provided in Section IV, the most favorable PMVM configuration among the two examined types was found to be the overlap-winding PMVM as it generally possesses better power factor and lower torque ripples. The main properties of the two compared machines are described in Table IV and their cross sections are provided in Fig. 6. In addition, the two generators' detailed dimensional parameters are also given in Table V. In accordance with the different physical sizes of the machines, the air-gap lengths also differ since they are expressed as the percentage ratios of the total diameters.

For the PMVM, it was realized during the optimization process that the total active mass varies greatly with the aspect ratio. Therefore, the influence of this variable on total active mass at a 15-kW level was investigated on a machine with $p_s = 3$, $p_r = 33$, and $Q = 36$. As can be read from Fig. 7, the PMVM's mass is high at very low aspect ratios, but this tends to decrease with increasing (L_{stk}/D_{out}) values. From 0.4 to 0.6, the mass remains almost constant, which means that an aspect ratio close to 0.4 would be a good choice for this machine.
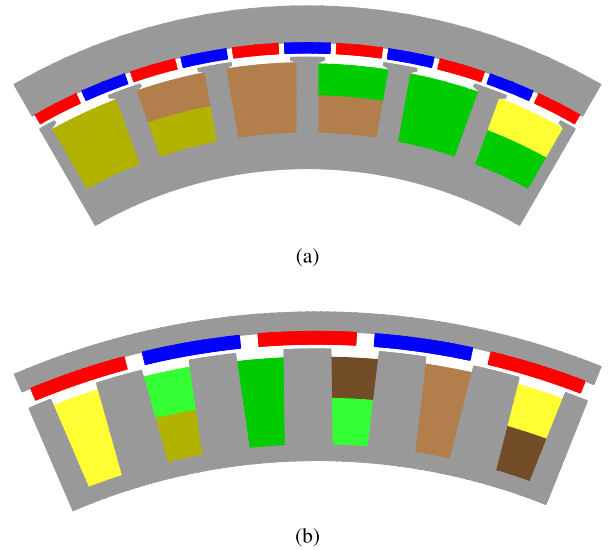

Fig. 6. Machine cross sections: (a) PMVM and (b) PMSM.

While the overall mass of the machine is an important aspect for the intended application, the cost per kilogram of PM material is usually high, hence it has a significant contribution to the cost of the machine. On the other hand, machines with higher PM mass tend to have high power factors, which is beneficial in terms of the power converter cost. These relationships were explored, as shown in Figs. 8 and 9, in order to select a design

TABLE V
MACHINES' DIMENSIONAL PARAMETERS

Parameter	PMSM	PMVM
Rotor yoke height (t_{ry})	8.3 mm	13.6 mm
Rotor magnet height (t_{mh})	5.5 mm	3.9 mm
Magnet pole span (σ_{pm})	0.84	0.88
Air-gap length (g)	2 mm	1.5 mm
Stator yoke height (t_{sy})	6.7 mm	13.6 mm
Stator slot angle ratio (σ_s)	0.51	0.74
Slot opening ratio (σ_{so})	1.0	0.82
Stator tooth length (l_{st})	41.0 mm	27.96 mm
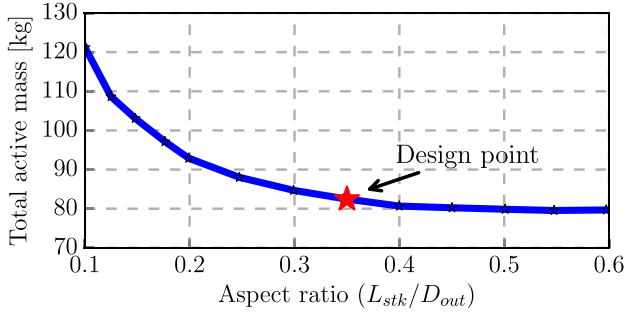
Fig. 7.   PMVM total active mass versus aspect ratio.
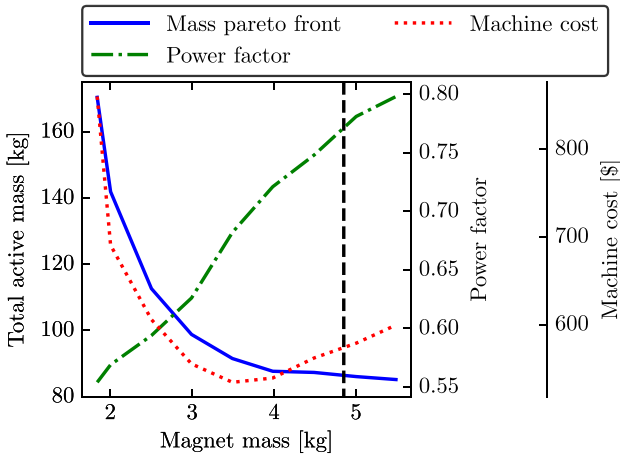

Fig. 8.   PMVM mass, power factor, and active material cost as a function of permanent magnet mass for constant efficiency of 94%.

point that is sensible from a system perspective. In Fig. 8, it is clear that low PM material usage renders the heaviest machine with the worst power factor. With an increase of the PM mass, the total active mass rapidly decreases before it gets stagnant at 4.0 kg of PM mass and beyond. The machine's active material cost has a minimum at moderate PM material usage. However, increasing the PM usage further continues to improve the power factor such that the system cost almost remains constant, as seen in Fig. 9, where the system cost was calculated as the sum of the machine's active material cost and the converter cost. The required converter rating was calculated as the rated power (15 kW) divided by the machine's power factor.

Accurate estimation of the power converter cost is a difficult task which depends on many factors besides the kVA rating.
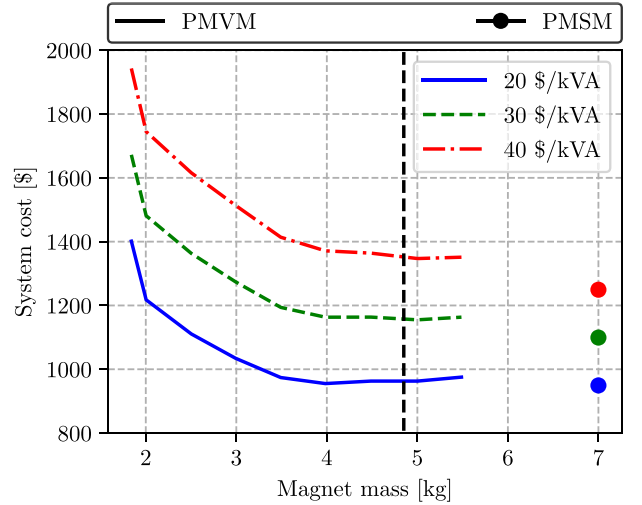

Fig. 9.   Comparison of system costs versus permanent magnet mass for different converter cost levels.

Other factors that influence the cost include the required switching and output fundamental frequencies, load characteristics, acceptable ripple current, required efficiency, and cooling. In Fig. 9, three different scenarios are shown, assuming that the converter cost scales linearly with the kVA rating. As described, this is a rough simplification. Practically, converter costs for this application may rather follow a stepped curve that climbs significantly slower than linearly. Thus, it is likely that PMVM system costs shown in Fig. 9 are overestimated relative to that of the PMSM system costs. Nevertheless, the data shown in Fig. 9 is sufficient to conclude that the PMSM and PMVM system costs will be comparable for the range of converter costs considered. Furthermore, it enables a good choice regarding the tradeoff between low magnet mass, low total mass, and high power factor to be made. A design point indicated by the vertical dashed lines in Figs. 8 and 9 was selected where the machine is light, has an acceptable power factor, and the system cost is low.

B. FE Demagnetization Analysis of Selected PMVM

Permanent magnet demagnetization is one important design aspect that needs special consideration in PM excited machines, especially those with the surface-mounted PM rotors. The risk of demagnetization is influenced by several operational factors including the PM's thermal state, machine overload, or faulty conditions. One potentially damaging scenario is during a fault, where large negative d-axis currents create a strong magnetic field opposing that of the PMs. Therefore, simple demagnetization checks on the designed PMVM were performed to evaluate the risk of demagnetizing the PMs under the different operating conditions. The operating conditions considered correspond to full-load operation and operation with rated current on the negative d-axis and twice rated current on the negative d-axis. Fig. 10 shows the demagnetization proximity for the different conditions, where the demagnetization proximity is defined as the margin to the knee point of the demagnetization curve. For the designed PMVM, little difference is observed when
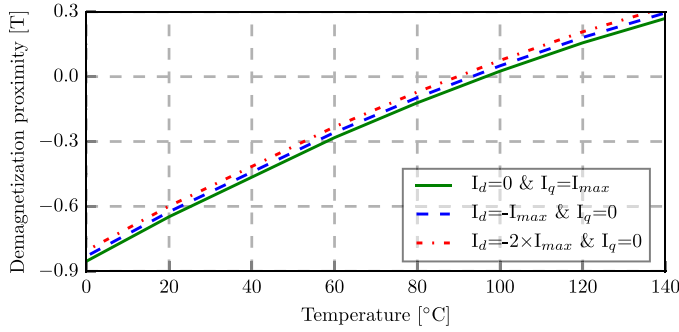
Fig. 10. PMs' demagnetization proximity at different temperature conditions.

TABLE VI
VOLUME, COST, AND WEIGHT DETAILS OF PMSM AND PMVM

Parameter	PMSM	PMVM
Outer diameter (D_{out})	655 mm	433 mm
Stack length (L_{stk})	125 mm	151 mm
End-winding overhang	23 mm	66 mm
Inner diameter (D_i)	528 mm	313 mm
Torque density (kNm/m^3)	23.7	45.6
Torque per active volume (kNm/m^3)	68.5	98.1
Torque per active mass (Nm/kg)	11.2	12.0
PM mass ($50/kg)	7.8 kg	4.85 kg
Silicon steel mass ($2/kg)	62.44 kg	45.08 kg
Copper mass ($6.67/kg)	20.16 kg	34.49 kg
Total mass	89.6 kg	84.42 kg
Total active material cost	649 $	563 $

TABLE VII
PERFORMANCE CHARACTERISTICS OF PMSM AND PMVM

Parameter	PMSM		PMVM	
	FEA	Measured	FEA	Measured
Average torque (Nm)	1011.1	1060.0	1042.0	1038.23
Torque ripple (%)	3.42	–	1.25	3.45
Cogging torque (%)	2.34	2.84	1.66	1.80
Winding losses (W)	588.48	599.1	480.4	570.2
Core & PM losses (W)	245.4	–	476.4	–
Power factor (p.u.)	0.97	0.99	0.78	0.71
Output power (kW)	15.0	15.5	15.4	15.2
Efficiency (η %)	94.44	93.58	94.20	93.20
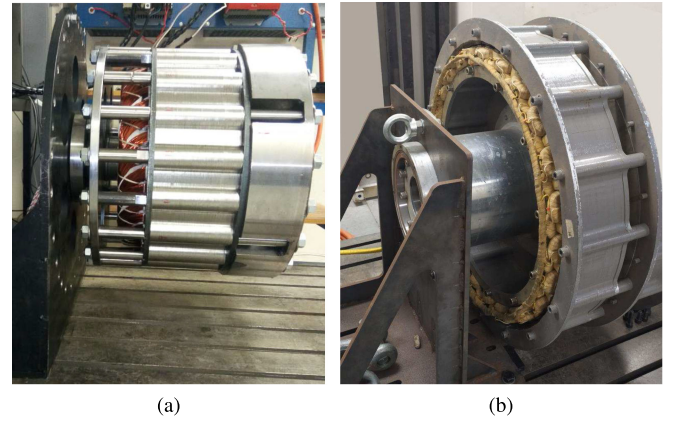
Fig. 11. Machine prototypes: (a) PMVM and (b) PMSM.

changing the current angle from normal operating conditions to the negative d-axis. However, the temperature has a significant influence on the proximity to demagnetization as the position of the knee point of the demagnetization curve moves up with increasing temperature. From Fig. 10, it is concluded that the PMVM machine would operate safely for any temperatures below 80 °C.

C. PMVM and PMSM Experimental Comparison

Regarding the comparison of the PMSM and PMVM, from Table VI, an estimation of the active volumetric machine size can be given by the total diameter (D_{out}) and active stack length (L_{stk}). While the active volume of the PMVM is about 60% of that of the PMSM, the total volume of the PMVM is close to 72% of the PMSM when taking into account their respective end-winding overhangs. Even though the PMVM has about 50% more armature winding mass than the PMSM, due to its long end-winding, it still has slightly lower overall total active mass than its counterpart. Moreover, it uses approximately 38% less PM material than PMSM. Output efficiencies are almost equal since this was the minimum constraint for the design optimization. The PMSM has a high power factor, which is normal for synchronous PM machines, whereas the PMVM has a lower power factor of 0.78. This is a known disadvantage for PMVMs, and with the above-indicated power factors, a power converter with higher kVA rating is necessary. As a result,

the PMVM's lower cost merit will be somewhat discounted. Cogging and torque ripple are two other critical factors in PM machines, as they can affect the machine's starting capability and also create adverse mechanical vibration and noise. The PMVM has smoother torque output than the PMSM as evidenced in Table VII.

The PMVM and benchmark PMSM prototypes are shown in Fig. 11. While the PMSM has a relatively shorter stack and winding overhang axial length, the PMVM has a smaller diameter, and ultimately, less volume. Since the two machines have an almost equivalent average torque output, it implies that the PMVM's torque density is superior to that of the PMSM.

A laboratory test setup is shown in Fig. 12. The drive system consisting of the induction machine as a prime mover to the prototype and the back-to-back converter for power conditioning and circulation was implemented for studying the performance of the prototype in generator mode. Due to the low torque ratings of the induction machine, a 1:7.6 ratio mechanical gearbox was used to step-up its output torque to satisfy the torque requirements of the prototype machines at rated conditions. Field-oriented control based on the dq-theory in the rotor reference frame is used to achieve the maximum torque at each stator current loading. This is performed with the aid of the position encoder attached to the rotor shaft, providing the controller with the rotor's speed and angular position at every time instant.

The measured cogging torque and FEA-predicted torque ripple waveforms are compared in Figs. 13 and 14, where it can
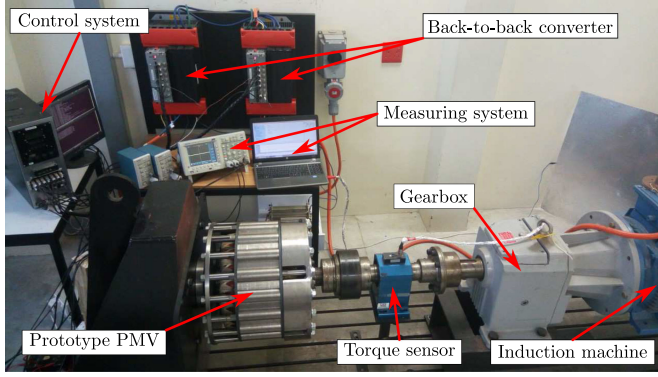
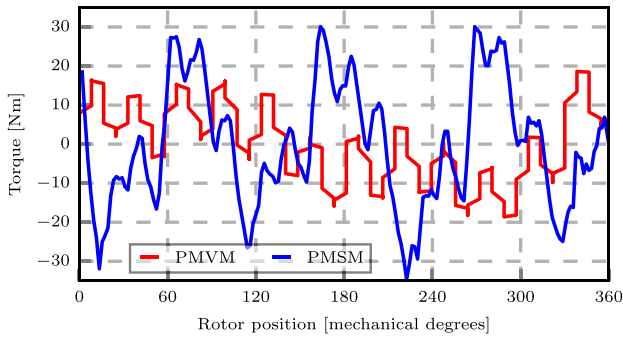Fig. 12. Experimental setup for the testing of 15 kW PMVM.

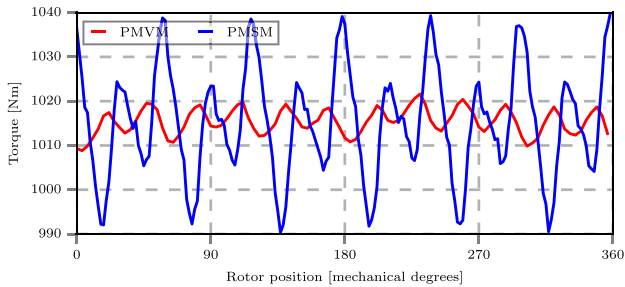Fig. 13. Measured cogging torques of PMVM and PMSM prototypes.

Fig. 14. Predicted torque ripples of both PMVM and PMSM machines.

Fig. 15. Open-circuit voltage waveforms: (a) PMVM; (b) PMSM; and (c) harmonics.
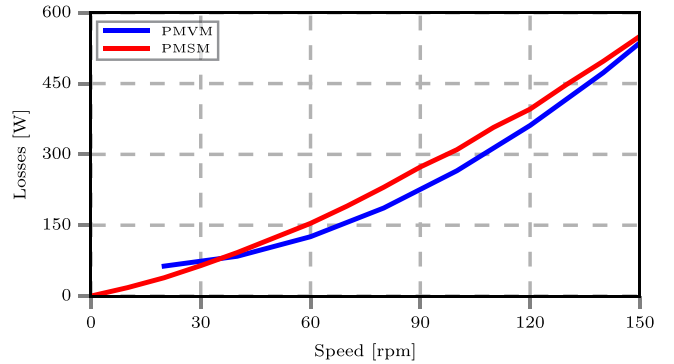
Fig. 16. Measured no-load losses of the PMVM and PMSM prototypes.

be seen that the PMVM has smaller cogging and smoother average torque characteristics than the PMSM. Their magnitudes are further in good agreement with the percentage indications on Table VII. On the other hand, the line-to-line open-circuit voltage waveforms are almost sinusoidal with the presence of small higher order harmonics as indicated by Fig. 15. The difference between the measured and FEA-predicted voltage characteristics is insignificant. In terms of the percentages, the higher order harmonics are all less than 2%. Therefore, the minimum harmonic content clearly proves that both machines have good voltage quality.

Fig. 16 shows the measured no-load losses versus rotor-speed for the PMVM and PMSM, respectively. Even though they operate at different rated frequencies, there is a negligible differ-ence between the two machines' practical losses at lower input
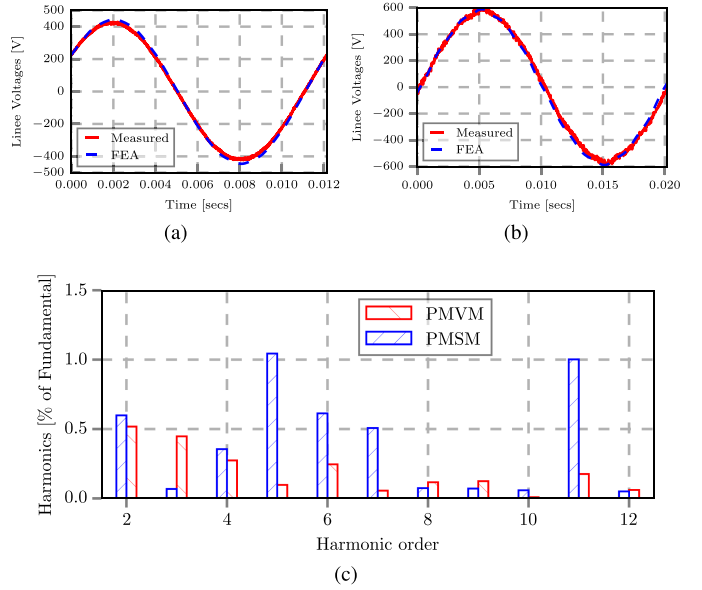
speeds up to 150 r/min. That is, the influence of PMVM's higher frequency on eddy-current and hysteresis losses seems to be offset by its lower PM and silicon–steel material content.

The power factors of the two machines as a function of their torque loading are presented in Fig. 17. The PMSM's power factor is generally very high under different torque loading, whereas the PMVM's power factor constantly decreases from above 0.95 to 0.71 with increasing torque loads. At rated torque condition, the PMVM achieves a power factor of 0.71, which is less than the FE-predicted value of 0.78.

The efficiency versus the output power of the two machine types is provided in Fig. 18. Both machines show a fairly good efficiency in the region above 50% of the rated power. Due to the relatively high losses in the machines as indicated in Fig. 16, both machines' efficiencies are also reduced from above 94% to just above 93% at full rated power of 15 kW. The difference between the FE-predicted and measured results can be attributed to the construction imperfections, inaccurate core-loss model, and unaccounted harmonic losses.
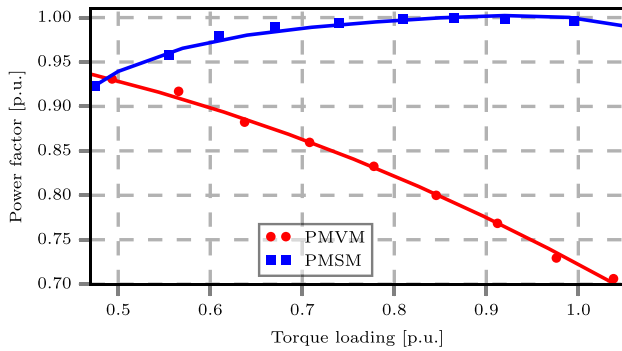
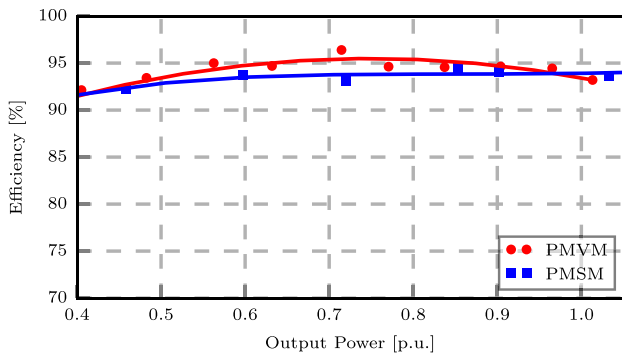Fig. 17.   Output power factor with respect to machines' torque loading.

Fig. 18.   Machines' efficiencies as a function of output power.

VI. CONCLUSION

A comparative study between two surface-mounted PM machines, a PMSM and a PMVM, has been conducted in this article. Since the PMSM was already existing and taken as the comparison benchmark, the study began by designing the PMVM with more emphasis placed on the effect of pole ratio on certain performance indexes. It was shown that careful consideration needs to be applied when choosing the pole/slot combination of PMVM because that is one of the major determining factors for the machine's total active mass, power factor, and torque quality. From the comparison results, the designed PMVM has a clear advantage of lower PM material requirement while also boasting on the torque density. Both machines have good torque quality, but the PMVM's is better and was achieved without applying any special techniques to improve torque quality. On the other hand, the PMSM has a good power factor which makes it superior in terms of the size and cost of the converter relative to the PMVM. However, the overall cost of PMVM wind generation system is still comparable with that of the PMSM system at 15 kW power level.

For validation purposes, a 15-kW PMVM was successfully constructed and tested, which is currently the largest PMVM prototype according to the literature. The measured results of the PMVM and PMSM are compared, which shows that the PMVM can be deemed a reasonable alternative to its PMSM counterpart at the investigated output power level.

REFERENCES

[1] G. Shrestha, H. Polinder, and J. A. Ferreira, "Scaling laws for direct drive generators in wind turbines," in *Proc. IEEE Int. Elect. Mach. Drives Conf.*, May 2009, pp. 797–803.
[2] H. Li and Z. Chen, "Overview of different wind generator systems and their comparisons," *IET Renewable Power Gener.*, vol. 2, no. 2, pp. 123–138, Jun. 2008.
[3] H. Polinder, F. Van der Pijl, G.-J. de Vilder, and P. Tavner, "Comparison of direct-drive and geared generator concepts for wind turbines," in *Proc. IEEE Int. Conf. Elect. Mach. Drives*, 2005, pp. 543–550.
[4] B. Kim, "Design method of a direct-drive permanent magnet vernier generator for a wind turbine system," *IEEE Trans. Ind. Appl.*, vol. 55, no. 5, pp. 4665–4675, Sep./Oct. 2019.
[5] P. M. Tlali, R-J. Wang, and S. Gerber, "Comparison of PM vernier and conventional synchronous 15 kW wind generators," in *Proc. Int. Conf. Elect. Mach.*, Sep. 2018, pp. 2065–2071.
[6] R. Zeinali and H. B. Ertan, "Comparison of a magnetically geared PM wind generator with radial flux generator," in *Proc. 7th Int. Conf. Rel., Infocom Technol. Optim. (Trends Future Directions)*, Noida, India, 2018, pp. 1–10.
[7] B. Kim and T. A. Lipo, "Operation and design principles of a PM vernier motor," *IEEE Trans. Ind. Appl.*, vol. 50, no. 6, pp. 3656–3663, Nov./Dec. 2014.
[8] Y. Yu, F. Chai, Y. Pei, and L. Chen, "Comparison of torque performance in surface-mounted PM vernier machines with different stator tooth topologies," *IEEE Trans. Ind. Appl.*, vol. 55, no. 4, pp. 3671–3684, Jul./Aug. 2019.
[9] J. Li and K. Chau, "Performance and cost comparison of permanent-magnet vernier machines," *IEEE Trans. Appl. Supercond.*, vol. 22, no. 3, Jun. 2012, Art. no. 5202304.
[10] W. Fu and S. Ho, "A quantitative comparative analysis of a novel flux-modulated permanent-magnet motor for low-speed drive," *IEEE Trans. Magn.*, vol. 46, no. 1, pp. 127–134, Jan. 2010.
[11] C. Liu, C. H. Lee, and M. Chen, "Comparison of outer-rotor permanent magnet machines for in-wheel drives," in *Proc. IEEE Int. Symp. Ind. Electron.*, May 2013, pp. 1–6.
[12] S. Gerber and R.-J. Wang, "Design and evaluation of a PM vernier machine," in *Proc. IEEE Energy Convers. Congr. Expo.*, Sep. 2015, pp. 5188–5194.
[13] Z. S. Du and T. A. Lipo, "Torque performance comparison between a ferrite magnet vernier motor and an industrial interior permanent magnet machine," *IEEE Trans. Ind. Appl.*, vol. 53, no. 3, pp. 2088–2097, May/Jun. 2017.
[14] B. Kim and T. A. Lipo, "Design of a surface PM vernier motor for a practical variable speed application," in *Proc. IEEE Energy Convers. Congr. Expo.*, Sep. 2015, pp. 776–783.
[15] A. Toba and T. A. Lipo, "Generic torque-maximizing design methodology of surface permanent-magnet vernier machine," *IEEE Trans. Ind. Appl.*, vol. 36, no. 6, pp. 1539–1546, Nov./Dec. 2000.
[16] S. E. Skaar, Ø. Krøvel, and R. Nilssen, "Distribution, coil-span and winding factors for PM machines with concentrated windings," in *Proc. Int. Conf. Elect. Mach.*, Sep. 2006, Paper 346.
[17] F. Libert and J. Soulard, "Investigation on pole-slot combinations for permanent-magnet machines with concentrated windings," in *Proc. Int. Conf. Elect. Mach.*, Sep. 2004, Paper 530.
[18] Vanderplaats Resarch & Development, Inc, "Theory manual," Jun. 2013. [Online]. Available: http://www.vrand.com/visualDOC.html
[19] D. Li, R. Qu, and T. A. Lipo, "High-power-factor vernier permanent-magnet machines," *IEEE Trans. Ind. Appl.*, vol. 50, no. 6, pp. 3664–3674, Nov./Dec. 2014.
[20] Z. Q. Zhu and D. Howe, "Influence of design parameters on cogging torque in permanent magnet machines," *IEEE Trans. Energy Convers.*, vol. 15, no. 4, pp. 407–412, Dec. 2000.
[21] S. Hyoseok, N. Niguchi, and K. Hirata, "Characteristic analysis of surface permanent-magnet vernier motor according to pole ratio and winding pole number," *IEEE Trans. Magn.*, vol. 53, no. 11, Nov. 2017, Art. no. 8211104.
[22] L. Wu, R. Qu, D. Li, and Y. Gao, "Influence of pole ratio and winding pole numbers on performance and optimal design parameters of surface permanent-magnet vernier machines," *IEEE Trans. Ind. Appl.*, vol. 51, no. 5, pp. 3707–3715, Sep./Oct. 2015.
[23] J. H. J. Potgieter and M. J. Kamper, "Design optimization of directly grid-connected PM machines for wind energy applications," *IEEE Trans. Ind. Appl.*, vol. 51, no. 4, pp. 2949–2958, Jul./Aug. 2015.

Pushman M. Tlali (Member, IEEE) was born in Leribe, Lesotho. He received the B.Eng. degree in electrical and electronic engineering in 2012, and the M.Eng. and Ph.D. degrees in electrical engineering from Stellenbosch University, Stellenbosch, South Africa, in 2015 and 2019, respectively.

He is currently a Postdoctoral Research Fellow with the same university. His research interests include the design and optimization of rotating electrical machines with a specific focus on magnetically geared PM machines, and renewable energy power generation.

Rong-Jie Wang (Senior Member, IEEE) received the M.Sc. degree in electrical engineering from the University of Cape Town, Cape Town, South Africa, in 1998, and the Ph.D. degree in electrical engineering from Stellenbosch University, Stellenbosch, South Africa, in 2003.

He is currently an Associate Professor with the Department of Electrical and Electronic Engineering, Stellenbosch University. In recent years, his work has been focused on the magnetic gear and magnetically geared electrical machine technologies. His research interests include novel topologies of permanent magnet machines, computer-aided design and optimization of electrical machines, cooling design and analysis, and renewable energy systems.

Stiaan Gerber (Member, IEEE) received the Ph.D. degree in electrical engineering from Stellenbosch University, Stellenbosch, South Africa, in 2015.

He is currently a Postdoctoral Researcher with the same university. He is an avid software developer and has published more than 20 papers in recognized international journals and conference proceedings. His research interests in the engineering field include electrical machine design, magnetic gear technology, numerical optimization, finite-element methods, and renewable power generation.

Christoff Daniel Botha received the B.Eng. and M.Eng. degrees in electrical and electronic engineering in 2015 and 2018, respectively, from Stellenbosch University, Stellenbosch, South Africa, where he is currently working toward the Ph.D. degree with the Department of Electrical and Electronic Engineering.

His research interests include the design and optimization of electric machines and energy storage for use in renewable energy grid integration.

Maarten J. Kamper (Senior Member, IEEE) received the M.Sc. (Eng.) and Ph.D. (Eng.) degrees in the field of design of induction and reluctance electrical machines from the University of Stellenbosch, Stellenbosch, South Africa, in 1987 and 1996, respectively.

Since 1989, he has been with the Department of Electrical and Electronic Engineering, University of Stellenbosch, where he is currently a Professor of Electrical Machines and Drives. His research interests include the design optimization and control of electrical machines, currently with the focus on wind generators, synchronous condensers, and industrial and electric vehicle drives.

Prof. Kamper is a registered Professional Engineer in South Africa.